

LpQcM: Adaptable Lesion-Quantification-Consistent Modulation for Deep Learning Low-Count PET Image Denoising

Menghua Xia, *Member, IEEE*, Huidong Xie, *Student Member, IEEE*, Qiong Liu, *Student Member, IEEE*, Bo Zhou, *Student Member, IEEE*, Hanzhong Wang, Biao Li, Axel Rominger, Kuangyu Shi, Georges El Fakhri, *Fellow, IEEE*, and Chi Liu, *Senior Member, IEEE*

Abstract—Deep learning-based positron emission tomography (PET) image denoising offers the potential to reduce radiation exposure and scanning time by transforming low-count images into high-count equivalents. However, existing methods typically blur crucial details, leading to inaccurate lesion quantification. This paper proposes a lesion-perceived and quantification-consistent modulation (LpQcM) strategy for enhanced PET image denoising, via employing downstream lesion quantification analysis as auxiliary tools. The LpQcM is a plug-and-play design adaptable to a wide range of model architectures, modulating the sampling and optimization procedures of model training without adding any computational burden to the inference phase. Specifically, the LpQcM consists of two components, the lesion-perceived modulation (LpM) and the multiscale quantification-consistent modulation (QcM). The LpM enhances lesion contrast and visibility by allocating higher sampling weights and stricter loss criteria to lesion-present samples determined by an auxiliary segmentation network than lesion-absent ones. The QcM further emphasizes accuracy of quantification for both the mean and maximum standardized uptake value (SUV_{mean} and SUV_{max}) across multiscale sub-regions throughout the entire image, thereby enhancing the overall image quality. Experiments conducted on large PET datasets from multiple centers and vendors, and varying noise levels demonstrated the LpQcM efficacy across various denoising frameworks. Compared to frameworks without LpQcM, the integration of LpQcM reduces the lesion SUV_{mean} bias by 2.92% on average and increases the peak signal-to-noise ratio (PSNR) by 0.34 on average, for denoising images of extremely low-count levels below 10%. (Code will be available at <https://github.com/mhxiaaa/LpQcM-for-PET-image-denoising>)

Index Terms—Low-count PET image denoising, deep learning, segmentation-assisted denoising, lesion quantification.

I. INTRODUCTION

Positron emission tomography (PET) is a highly sensitive nuclear medicine imaging technique that can visualize functional processes in the body through injected radiotracers [1]. Its application spans a wide range of medical fields, including oncology, neurology, and cardiology, playing a crucial role in disease diagnosis and follow-up therapy [2]. The noise level of PET images is primarily determined by counts of

detected photon events, which are influenced by two main factors: the ionization burden (injected tracer dose) on patients and the efficiency of the scanning system hardware. Minimizing radiation exposure in line with the principle of As Low As Reasonably Achievable (ALARA) [3] or reducing hardware expenses will result in low-count artifactual images of high noises, compromising the diagnostic accuracy. To tackle this tradeoff between high-quality imaging and constraints imposed by clinical safety and economic considerations, software denoising algorithms are developed to remove noises and enhance the quality of low-count images.

Published PET image denoising algorithms encompass both conventional and deep learning (DL) approaches [4]. Conventional methods consist of dedicatedly designed filters, such as the non-local mean (NLM) filter with spatiotemporal enhancements [5], the multiple-reconstruction NLM (MR-NLM) filter that leverages the redundant information from multiple PET reconstructions [6], wavelet transforms enhanced by anatomical knowledge [7], multiresolution curvelet transforms [8], and integrated wavelets and curvelets [9]. In recent years, DL denoising methods for PET images have thrived and outperformed conventional ones [10]. These DL models typically utilize paired low-count and high-count PET images as training datasets to learn a mapping function that translates low-count images into their high-count equivalents. These methods vary in their adopted network architectures, including convolutional neural networks (CNNs) [11][12][13], generative adversarial networks (GANs) [14], and vision transformers (ViTs) [15]. Additionally, several models arm the denoising framework with added functionalities, such as embedding noise-aware mechanisms to adaptively handle varying low-count noise levels [16][17], deploying federated deep transformation networks to address privacy issues across multiple institutions [18], and utilizing magnetic resonance-guided fusion modules to exploit cross-modality information thereby boosting performance [19][20]. The latest advances involve integrating deep networks with traditional iterative optimization models [21] and exploring diffusion probabilistic models for PET denoising [22][23][24], both showing promising future potential.

This work was supported by the National Institutes of Health (NIH) under grant R01CA275188. Corresponding author: Chi Liu (email: chi.liu@yale.edu). Menghua Xia, Georges El Fakhri, and Chi Liu are with the Department of Radiology and Biomedical Imaging, Yale University School of Medicine, New Haven, CT, USA.

Huidong Xie, Qiong Liu, Bo Zhou, and Chi Liu are with the Department of Biomedical Engineering, Yale University, New Haven, CT, USA. Hanzhong Wang and Biao Li are with the Department of Nuclear Medicine, Ruijin Hospital, Shanghai Jiao Tong University School of Medicine, Shanghai, China.

Axel Rominger and Kuangyu Shi are with the Department of Nuclear Medicine, Inselspital, Bern University Hospital, University of Bern, Bern, Switzerland. Kuangyu Shi is also with the Computer Aided Medical Procedures and Augmented Reality, Institute of Informatics 116, Technical University of Munich, Munich, Germany.

Although current DL methods for PET image denoising achieve visually appealing results, they tend to over-smooth images with diminished structural details. Consequently, the quality of denoised images could be insufficient for lesion detection and accurate radioactivity quantification. Typically, lesions appear with reduced contrast in denoised images or may even be erroneously omitted, causing under-estimations on clinical metrics such as the standard uptake value (SUV), as detailed in [25][26]. Occasionally, DL models could be misled by significant noises and generate false-positive lesions that do not actually exist [25][26], which results in quantification over-estimations. This issue of over-smoothing and lesion quantification inaccuracy in PET image denoising hinders the clinical applications of DL technologies.

To address this challenge, it's intuitive to consider employing either manually annotated lesion labels or automated lesion segmentation to facilitate the denoising process. Yet, to the best of our knowledge, no DL denoising method that incorporates this concept has been proposed for PET imaging. This oversight could be attributed to the significant difficulty in labeling lesion regions or acquiring datasets that include matched lesion labels for low- and high-count images. While some approaches for other medical imaging modalities have explored combining denoising with segmentation, they struggle to adapt to PET scenarios. For instance, networks integrating prior anatomical knowledge have been developed for low-dose CT denoising [27][28][29], where the anatomical information is derived from a subnetwork tasked with organ segmentation and characterization. Similarly, the DenoiSeg model [30], tailored for microscopy image analysis, leverages a single Unet with four output channels to concurrently perform both self-supervised denoising and supervised segmentation. Its multi-channel output delivers both denoised images and segmentation masks. These segmentation-assisted denoising approaches fit in situations where target objects occupy a relatively large area in images. They are not well-suited for PET cases where the targets, i.e., metabolically active lesions, may be extremely small (e.g., less than 150 voxels in an image of $440 \times 440 \times 644$ voxels, or 674 mm^3 out of $5.6 \times 10^8 \text{ mm}^3$). Additionally, methods [27][28][29] rely on cascaded attention modules to fuse features from segmentation branches into the denoising network, complicating the primary denoising architecture and consequently increasing computational burden and inference time. The DenoiSeg model [30], while simple, is primarily focused on segmentation, treating denoising as a secondary task without an emphasis on denoising efficacy. Moreover, all these approaches use a denoising-segmentation-coupled design, which necessitates matched manual segmentation labels for noisy and clean image pairs in denoising datasets. The difficult access to these kinds of datasets might be the reason hindering the emergence of similar methods in PET.

In this study, to address the challenge of retaining lesion quantification accuracy in PET image denoising and to facilitate smooth deployment on DL models, we introduce the **lesion-perceived and quantification-consistent modulation (LpQcM)** strategy. Major contributions are as follows:

(1) The LpQcM utilizes auxiliary lesion segmentation and quantification to aid DL-based PET image denoising. It avoids the need for manual lesion labels in denoising datasets, by decoupling the auxiliary analysis from the main denoising process and pre-training the auxiliary tool on public sources. This design makes the LpQcM a versatile plug-and-play module compatible with a wide range of DL frameworks. Additionally, the LpQcM operates only during model training, adjusting sampling and optimization procedures without adding computational burden to model inference.

(2) The LpQcM introduces two novelties: lesion-perceived modulation (LpM) and multiscale quantification-consistent modulation (QcM). The LpM leverages the pre-trained lesion segmentation network to enhance lesion visibility and lesion quantification accuracies. The QcM further demands precise radioactivity quantifications on multiscale sub-regions across the entire image, thus improving overall image quality with mitigated over-smoothing.

(3) Extensive experiments were conducted on large datasets from multiple medical centers, major vendor scanners, and various low-count noise levels. First, the LpQcM effectiveness in enhancing lesion visibility and image quality was proven on Unet baseline. Then, detailed ablation studies illustrated individual contributions of each LpQcM component. Finally, the flexible applicability of the LpQcM across various denoising frameworks was demonstrated.

II. METHODS

Fig. 1 illustrates the proposed method. The LpQcM operates solely during the training phase and is omitted in the inference. In terms of the denoising baseline, various network architectures can be selected. As a large-size 3D PET image cannot be processed as a whole due to computational limitations, it is systematically processed patch by patch. Let I_{LC} / I_{HC} denote the low/high-count PET image pairs. The denoising network $f_{den}(\cdot)$ is trained under supervisions of extracted low/high-count patch pairs V_{LC}/V_{HC} and the guidance of the LpQcM. In the inference stage, the trained $f_{den}(\cdot)$ maps low-count patches V_{LC} into denoised ones V_{DEN} , which are then reassembled into the denoised PET image I_{DEN} . Details are as below.

A. Lesion-Perceived Modulation

The first component of the LpQcM, the LpM, is designed to enhance the lesion contrast and visibility in denoised images. To accomplish this, the LpM incorporates a segmentation network $f_{seg}(\cdot)$ to identify lesion regions.

Given that the lesion segmentation serves as an auxiliary task to support the denoising process without requiring perfect accuracy, the $f_{seg}(\cdot)$ within LpM adopts a simple and compact Unet architecture [31]. This design comprises a four-layer hierarchical encoder and a three-layer decoder, with the shallowest layer's feature channels set to 32. To promote feature learning and facilitate gradient flow, residual connections are employed at each encoder layer, while deep supervisions are deployed at each decoder layer. Before being integrated into the

denoising workflow, the $f_{seg}(\cdot)$ undergoes pre-training using public PET data sources (described in Section III-A) specifically curated for lesion segmentation tasks. Input the high-count patch V_{HC} , the trained $f_{seg}(\cdot)$ outputs the segmentation probability map $f_{seg}(V_{HC}(j)) \in [0,1]$, indicating the likelihood of each voxel j belonging to a lesion.

The LpM directly leverages lesion probability maps instead of their binarized masks, thus in a soft modulation way, to guide the denoising learning process to concentrate on lesions, through patch-level lesion-perceived sampling and voxel-level lesion-perceived consistency constraint.

1) Lesion-perceived sampling

After departing PET images into patches, a significant majority of these patches will not contain lesions, given that lesions are generally much smaller than the overall image size, as shown in the sample histogram of patch counts - lesion probability in Fig. 1. The imbalanced distribution of patches with and without lesions will skew DL algorithms toward predicting the majority type of lesion-absent patches, detrimentally affecting the denoising performance on actual lesions. To this end, the LpM designs a lesion-perceived sampling function to prioritize the minority yet crucial patches containing lesions. This function actively assigns greater sampling weights to lesion-present patches compared to lesion-absent ones, thereby mitigating the training data distribution imbalance between the lesion and non-lesion knowledge. The sampling weight for a training patch pair (V_{LC}, V_{HC}) is set as follows:

$$w(V_{LC}, V_{HC}) = \eta(V_{LC}) \cdot \max\left\{\max_j\{f_{seg}(V_{HC}(j))\}, w_{min}\right\} \quad (1)$$

where $f_{seg}(V_{HC}(j)) \in [0,1]$ is the lesion probability determined by the segmentation network on the high-count patch V_{HC} , signifying the likelihood of each voxel j being part of a lesion. The highest lesion probability within a patch, denoted as $\max_j\{f_{seg}(V_{HC}(j))\}$, indicates the presence of lesions in V_{HC} . To avoid lesion-absent patches of zero probabilities being entirely excluded from the sampling procedure, a minimum weight threshold, w_{min} , is established (0.3 in this study). Additionally, considering the varying noise levels in low-count PET images and the increased challenge in preserving lesion details from noisier images, we further modulate sampling weights by a noise-aware factor $\eta(V_{LC})$. This factor is inversely related to the count level of V_{LC} , increasing as the count level decreases (described in Section III-B).

In summary, patches with a higher likelihood of containing lesions alongside heavier background noises are deemed more critical and receive priority in the denoising learning process. Conversely, patches without lesions and less noise are selected less frequently, optimizing denoising model's focus and efficacy.

2) Lesion-perceived consistency constraint

Beyond the imbalance between the amounts of patches with lesions and those without, there also exists a disparity between lesional and non-lesional voxels. Often, in a patch identified as containing lesions, the majority of voxels are non-lesional. To

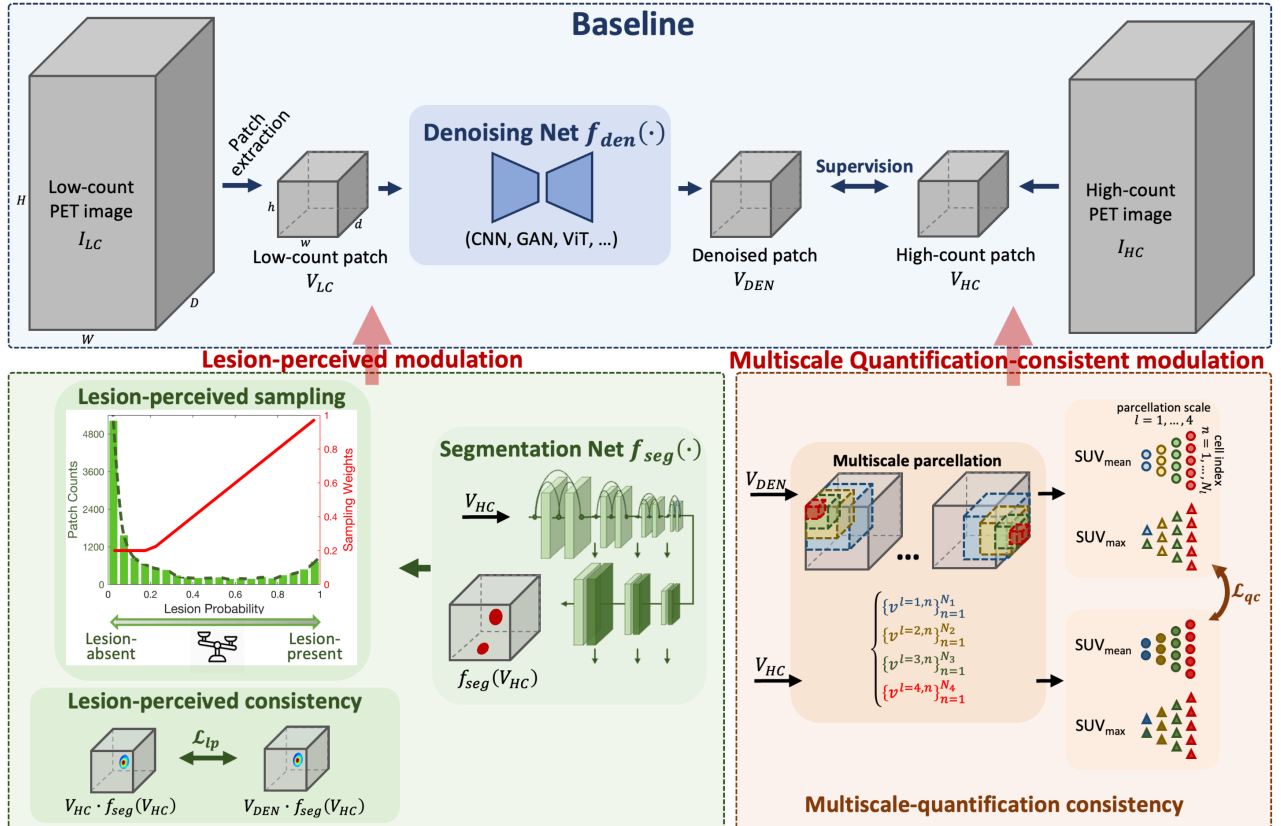


Fig. 1 Illustration of the proposed LpQcM strategy. The lesion-perceived modulation (LpM) and the multiscale quantification-consistent modulation (QcM) tune the sampling and optimization process of the denoising baseline during training.

further emphasize lesion preservation, the LpM introduces a lesion-perceived consistency constraint, \mathcal{L}_{lp} , providing more rigorous supervision over lesion voxels during the denoising process, as shown in Fig. 1. \mathcal{L}_{lp} is formulated as:

$$\mathcal{L}_{lp}(V_{DEN}, V_{HC}) = \frac{1}{J} \sum_{j=1}^J f_{seg}(V_{HC}(j)) \cdot |V_{DEN}(j) - V_{HC}(j)| \quad (2)$$

where J denotes the total number of lesion voxels determined by the segmentation network $f_{seg}(\cdot)$. \mathcal{L}_{lp} concentrates the optimization specifically on lesion areas and prioritizes voxels based on their probability of being lesional. It gives higher attention to voxels that are more likely to be part of lesions. Such a design ensures that within lesions the denoised output V_{DEN} aligns closely with the high-count reference V_{HC} voxel-by-voxel in terms of SUV. The emphasis on voxel-wise lesion SUV consistency also guarantees the accuracy of the total lesion glycolysis (TLG) metric [32], which is the multiplication of tumor volume and average SUV in tumor. Keeping the TLG accuracy during denoising is of great clinical importance.

B. Multiscale Quantification-Consistent Modulation

The second component of the LpQcM, the QcM, aims at preserving radioactivity quantification accuracy on any selected sub-regions across the entire image scope, thus improving overall image quality and mitigating over-smoothing. The QcM formulates this expectation into a loss function to guide denoising learning.

As illustrated in Fig. 1, the QcM performs a multiscale parcellation, where sub-volumes of different sizes slide in the PET image with overlaps, representing the image as a collection of numerous volumetric sub-regions of various sizes. Following this parcellation, a multiscale-quantification consistency constraint, \mathcal{L}_{qc} , is conducted on these sub-volumes. The \mathcal{L}_{qc} demands that across multiple parcellation scales, each sub-volume derived from the denoised output V_{DEN} matches in SUV_{mean} and SUV_{max} with its counterpart from the high-count reference V_{HC} , expressed as:

$$\mathcal{L}_{qc} = \sum_{l=1}^4 \frac{\mu_l}{N^l} \cdot \sum_{n=1}^{N^l} \left(\left| \frac{1}{j^{l,n}} \sum_{j=1}^{j^{l,n}} v_{DEN}^{l,n}(j) - \frac{1}{j^{l,n}} \sum_{j=1}^{j^{l,n}} v_{HC}^{l,n}(j) \right| + \left| \max_j v_{DEN}^{l,n}(j) - \max_j v_{HC}^{l,n}(j) \right| \right) \quad (3)$$

where $l = 1, 2, 3, 4$ denotes the parcellation scale indices. N^l represents the total number of sub-volumes at the l -th scale, with n as the index for individual sub-volume. $\{v_{DEN}^{l,n}\}$ and $\{v_{HC}^{l,n}\}$ are sub-volumes obtained from V_{DEN} and V_{HC} , respectively. $j^{l,n}$ indicates the total voxel count within $v_{HC}^{l,n}$, with j as the voxel index. The sub-volume size for parcellation at scales $l = 1, 2, 3, 4$ is determined as a fraction $(\frac{1}{2}, \frac{1}{4}, \frac{1}{8}, \frac{1}{16})$ of the patch dimension $h \times w \times d$. The sliding stride is configured to be half of the corresponding sub-volume size. The parameter μ_l denotes weights allocated for each scale. Considering that constraints on smaller sub-volumes also beneficially affect larger sub-volumes, the μ_l is set to (0.03, 0.07, 0.15, 0.75) for scales $l = 1, 2, 3, 4$, with the highest weight on finest parcellation.

C. Model-Adaptable Optimization

The LpQcM can be flexibly applied to various denoising baseline models. The overall optimization process for models utilizing CNNs and ViTs follows Eq. (4). For models based on GANs, the optimization adheres to Eq. (5).

$$\min \mathcal{L}: \mathcal{L} = \mathcal{L}_{base} + \lambda_{lp} \mathcal{L}_{lp} + \lambda_{qc} \mathcal{L}_{qc}$$

$$\mathcal{L}_{base} = \frac{1}{N} \sum_{j=1}^N \|V_{DEN}(j) - V_{HC}(j)\|_2 \quad (4)$$

$$\min_G \max_D (\mathcal{L} + \mathcal{L}_{GAN})$$

$$\mathcal{L}_{GAN} = \mathbb{E} \left[\log \left(1 - D(G(V_{LC})) \right) \right] + \mathbb{E} [\log D(V_{HC})] \quad (5)$$

\mathcal{L}_{base} adopts the L2 loss between the denoised output V_{DEN} and the high-count V_{HC} . N denotes the total voxel count in V_{DEN} , with j as the voxel index. λ_{lp} and λ_{qc} are scalar weights for corresponding terms \mathcal{L}_{lp} and \mathcal{L}_{qc} , respectively. In the context of GANs, G and D refer to the generator and the discriminator, respectively. \mathcal{L}_{GAN} is the adversarial loss [33] for gaming between G and D .

III. EXPERIMENTS

A. Materials

The proposed LpQcM was evaluated on four large-size datasets obtained from multiple medical centers and vendors. Dataset A, B, and C include pairs of low- and high-count PET images, specifically collected for the denoising task. Dataset D contains high-count PET images along with lesion labels, which serves the pre-training of our auxiliary lesion segmentation network. Details are as below and in Table I.

Dataset A was acquired at the Department of Nuclear Medicine, University of Bern, Switzerland [14]. It includes 209 ^{18}F -FDG subjects scanned on a Siemens Biograph Vision Quadra scanner. Low-count PET data at 1%, 2%, 5%, 10%, 25%, and 50% count levels were created by non-overlapping down-sampling the PET list-mode data. Within this dataset, 100, 10, and 99 subjects were randomly selected for training, validation, and testing, respectively. **Dataset B** was collected at Ruijin Hospital, Shanghai, China [14]. 320 ^{18}F -FDG subjects scanned on a United Imaging uExplorer scanner were included in this dataset. Similarly, low-count PET data with count levels of 1%, 2%, 5%, 10%, 25%, and 50% were produced through non-overlapping down-sampling of the PET list-mode data. From this dataset, 150 subjects were used for training, 15 for validation, and 155 for testing. **Dataset C** was obtained from the Yale-New Haven Hospital, USA [18]. It includes 200 ^{18}F -FDG subjects scanned on a Siemens Biograph mCT scanner. Low-count PET data at 5%, 10%, and 20% count levels were created by non-overlapping down-sampling the PET list-mode data. All subjects in Dataset C were exclusively used for testing, for assessing the generalizability of denoising methods to unseen datasets.

Dataset D is a publicly available PET lesion segmentation dataset [34], acquired at University Hospital Tübingen, Germany, using a Siemens Biograph mCT scanner. This dataset included 501 patient studies, each featuring at least one FDG-avid tumor lesion. An experienced radiologist and a nuclear medicine physician gave manual annotations, resulting in

image-paired segmentation masks.

TABLE I Details of used datasets.

	Dataset A	Dataset B	Dataset C	Dataset D
Medical center	University of Bern, Switzerland	Ruijin Hospital, China	Yale-New Haven Hospital, USA	University Hospital Tübingen, Germany
Vendor	Siemens Biograph Vision Quadra	United Imaging uExplorer	Siemens Biograph mCT	Siemens Biograph mCT
Average dose (MBq)	264.1±18.2	260.1±12.2	256.3±16.2	314.7±22.1
Image size (voxels)	440×440×644	360×360×674	440×440× \hat{h} *	440×440× \hat{h} *
Voxel size (mm³/voxel)	1.65×1.65×1.65	1.67×1.67×2.89	2.04×2.04×2.03	2.04×2.04×3
Low-count levels (%)	1,2,5,10,25,50	1,2,5,10,25,50	5,10,20	/
# cases	209	320	200	501
Train/Val/Test split	100/10/99	150/15/155	0/0/200	350/21/130

* \hat{h} depends on patient height.

B. Technical Details

All PET images underwent cropping pre-processes to remove the outermost background areas lacking informative content, minimizing effects of voxels outside the body. For network processing, the entire image was divided into patches using a patch size of 80×80×80 voxels and a stride size of 20×20×20 voxels. Following advice in [35] on training a one-size-fits-all denoiser, the noise-aware factor $\eta(V_{LC})$ used in the lesion-perceived sampling described in Eq. (1) was empirically set to 0.35, 0.25, 0.15, 0.12, 0.08, and 0.05 for low-count levels of 1%, 2%, 5%, 10%, 25%, and 50%. For the selection of hyperparameters λ_{lp} and λ_{qc} in loss functions, a range of values were searched in cross-validation and the setting $\lambda_{lp}/\lambda_{qc}=0.15/0.5$ was determined to yield the best performance.

The auxiliary lesion segmentation network $f_{seg}(\cdot)$ was firstly pre-trained using Dataset D with rich lesion information and 200 extra lesion-absent patches cropped from training sets in Dataset A and B. These extra patches were selectively extracted from areas surrounding the brain, bladder, and heart which are prone to be mistakenly identified as lesions by DL models [34]. Including these patches into segmentation training helps the network $f_{seg}(\cdot)$ reduce false positives and improve its generalizability to datasets from other sources. Note that the $f_{seg}(\cdot)$ along with its generated lesion labels are used solely during the training phase of the denoising model and are not required for denoising inference stage.

The LpQcM was deployed on three distinct denoising frameworks covering CNN, ViT, and GAN. Specifically, Unet [31] and SwinUNETR [36] were selected as representatives for CNN and ViT, respectively. In the GAN configuration, the generator and discriminator architectures adopted Unet and patchGAN [33], respectively. All models were implemented on PyTorch platform using two Nvidia A40 GPUs. The Adam optimizer with an initial learning rate of 10^{-4} was adopted. Learning rate was reduced by a factor of 0.1 if no decrease in loss was observed over five consecutive epochs. Training was terminated when the learning rate fell below 10^{-7} .

C. Evaluation Measures

We use three types of metrics to assess the PET image denoising performance.

The first type includes widely used image quality metrics [37]: the normalized root-mean-square error (NRMSE), peak signal-to-noise ratio (PSNR), and structural similarity index (SSIM). These metrics are employed to evaluate the overall quality of the denoised image I_{DEN} , in comparison to its corresponding high-count reference I_{HC} . Lower NRMSE values and higher PSNR and SSIM scores are preferred, indicating a closer resemblance to the high-count images and a higher level of image fidelity.

The second type assesses quantification biases in clinical metrics between I_{DEN} and I_{HC} , including SUV_{mean} and SUV_{max} for individual lesions, as well as TLG for each image. Lesion labels used for calculations are determined by the trained segmentation network $f_{seg}(\cdot)$ on I_{HC} , compensating for the absence of manually annotated lesion labels. Given that the focus is on evaluating denoising performance, perfectly accurate lesion labels may not be crucial for this evaluation, making network-generated labels adequate. Zero-approaching biases in lesion SUV_{mean} , SUV_{max} , and TLG are desirable, indicating higher credibility of denoised images for clinical usage.

The third type evaluates the lesion contrast and visibility in denoised image I_{DEN} , with the trained segmentation network $f_{seg}(\cdot)$ serving as a model observer. Applying $f_{seg}(\cdot)$ to both I_{DEN} and the reference I_{HC} , the Tversky index is computed between segmentations:

$$Tversky(S_{DEN}, S_{HC}) = \frac{|S_{DEN} \cap S_{HC}|}{|S_{DEN} \cap S_{HC}| + \alpha |S_{DEN} \setminus S_{HC}| + \beta |S_{HC} \setminus S_{DEN}|} \quad (6)$$

where $S_{DEN} = B(f_{seg}(I_{DEN}))$ and $S_{HC} = B(f_{seg}(I_{HC}))$ denote segmentations performed on I_{DEN} and I_{HC} , respectively. $B(\cdot)$ represents the binary thresholding by 0.5, obtaining binary segmentation masks from the lesion probability maps output by $f_{seg}(\cdot)$. α and β specify the penalties for false positives and false negatives, respectively. Tversky index with $\alpha = \beta = 0.5$ equals to the Dice coefficient. A higher Tversky index is expected, indicating better lesion visibility in denoised images.

D. Experimental setup

In Section IV-A, we demonstrate the effectiveness of the LpQcM in enhancing both image quality and quantification accuracy. Section IV-B presents evidence of improved lesion visibility attributed to the LpQcM. In Section IV-C, detailed ablation studies are conducted to illustrate individual contributions of each LpQcM component. Section IV-D validates the versatile applicability of the LpQcM across different baseline models.

IV. RESULTS

A. LpQcM Effectiveness

The comprehensive performance of the LpQcM is detailed in Table II, with Unet as the baseline. Results illustrate that the LpQcM significantly improves nearly all the metrics, across a

TABLE II Effectiveness of the LpQcM in PET image denoising, across multiple vendors and varying levels of noises. Metrics include NRMSE, PSNR, SSIM, lesion SUV_{mean} bias, SUV_{max} bias, and TLG bias.

Scanner	Quadra						uExplorer						mCT		
Count level	1%	2%	5%	10%	25%	50%	1%	2%	5%	10%	25%	50%	5%	10%	20%
NRMSE (*100) (l)															
low-count	0.8481	0.5624	0.3511	0.2526	0.1592	0.0964	1.8625	1.0644	0.6210	0.4413	0.2660	0.1604	1.1507	0.7841	0.5209
w/o	0.2784	0.2374	0.2114	0.1934	0.1297	0.0955	0.5676	0.4641	0.4035	0.2961	0.2197	0.1621	0.5187	0.4378	0.3499
w	0.2669†	0.2230†	0.1958†	0.1742†	0.1246†	0.0877†	0.5412†	0.4357†	0.3868†	0.2857†	0.2092†	0.1466†	0.5101†	0.4266	0.3415†
PSNR (t)															
low-count	53.4961	53.4911	53.1449	54.6006	57.7667	61.9195	42.7091	44.5541	47.7175	50.0617	53.9333	58.1161	44.4868	46.3245	48.9443
w/o	52.4049	53.8832	55.4240	56.6402	58.9028	61.4126	46.1538	48.2235	50.3518	52.0480	54.4314	57.9374	47.2848	47.3059	50.7311
w	52.7619†	54.0509†	55.7434†	56.8496†	59.1895†	62.2200†	46.8346†	48.6562†	50.7446†	52.2847†	54.9677†	58.0367†	47.2848	48.8987†	50.8573†
SSIM (t)															
low-count	92.2886	94.5432	97.9339	99.1522	99.7735	99.9185	89.3091	94.3202	97.4967	98.6552	99.4786	99.8083	92.6756	95.6410	97.7591
w/o	99.4449	99.4131	99.4788	99.6314	99.8079	99.8956	97.4582	97.7019	99.0498	99.2507	99.5903	99.7264	97.9522	98.4152	98.8941
w	99.4498†	99.6392†	99.4291	99.7688†	99.8669†	99.9307†	98.0159†	98.7499†	99.1205†	99.4399†	99.6735†	99.8218†	98.0908†	98.5878†	99.0030†
SUV_{mean} bias (%) (o)															
low-count	-2.8822	-0.4444	1.1894	1.7032	1.4877	1.0523	-4.7541	-0.7803	1.1795	1.3783	0.9172	0.8148	-4.1840	-1.9378	-1.0527
w/o	-20.9481	-15.1270	-9.4446	-6.6938	-3.8582	-3.2085	-34.0514	-25.0210	-15.9125	-11.0226	-7.3184	-5.9334	-19.6617	-14.1664	-9.9552
w	-17.1284†	-12.8401†	-8.4912†	-5.7111†	-3.1306†	-1.5572†	-28.7256†	-20.5913†	-12.7371†	-8.4706†	-4.1922†	-2.4942†	-18.1669†	-13.5234†	-9.2264†
SUV_{max} bias (%) (o)															
low-count	57.7432	30.3965	16.2407	10.9325	6.2048	3.2711	88.9435	38.5935	17.8630	10.9979	5.3988	2.9287	29.6763	16.2583	7.8810
w/o	-26.4726	-20.1771	-13.4684	-9.8163	-6.4737	-6.3182	-43.5183	-32.2974	-20.3556	-14.5857	-10.0812	-8.9423	-23.5507	-18.1284	-13.9182
w	-19.2738†	-15.1079†	-10.1806†	-6.9593†	-3.8085†	-2.5458†	-31.1324†	-28.7588†	-15.3502†	-10.4629†	-4.8479†	-2.9853†	-20.3535†	-16.1925†	-11.8361†
TLG bias (%) (o)															
low-count	-1.9630	-0.7420	0.1737	0.5447	0.5959	0.4689	-2.3620	0.1267	1.3815	1.3684	0.9205	0.7685	-1.6421	-0.7831	-0.4284
w/o	-5.1424	-3.7719	-2.4461	-2.0756	-1.3106	-1.0552	-13.6426	-8.9747	-5.4630	-3.5913	-2.4951	-2.0810	-5.6128	-3.9736	-2.8746
w	-3.9830†	-3.2613†	-2.3935	-1.6708†	-1.2814	-0.6921†	-10.0584†	-6.3318†	-3.4872†	-2.3212†	-1.2506†	-0.7435†	-4.5547†	-3.0537†	-2.1296†

† Indicates that the difference between groups without (w/o) and with (w) the LpQcM is statistically significant, with $P < 0.05$ based on the non-parametric Wilcoxon signed-rank test. (t), (l) and (o) represent expecting higher, lower, and zero-approaching values, respectively.

variety of scanners and noise levels. This improvement indicates contributions of the LpQcM to enhanced visual similarity with high-count references and more accurate lesion quantification in denoised images. Particularly, on images of extremely low count levels below 10%, the LpQcM reduces quantification biases in lesion SUV_{mean} , SUV_{max} , and TLG by average of 4.14%, 6.63%, and 2.78%, respectively.

Fig. 2 presents sample denoised images without and with the LpQcM. Without the LpQcM, denoised images frequently exhibit over-smoothing, leading to the detail lost and poor contrast in small lesions and areas resembling lesions. Incorporation of the LpQcM mitigates this over-smoothing effect and enhances the contrast of both lesions and lesion-resembling hot spots in denoised images, as shown in Fig. 2.

B. Improved Lesion Visibility

The LpQcM leads to improved lesion visibility in denoised images, as evidenced in Table III. Using the trained lesion segmentation network as a model observer, the segmentation on low-count images significantly deviates from that on high-count references, with notably low Tversky indexes of 0.40, 0.34, and 0.30 for coefficients $\alpha/\beta = 0.3/0.7$, $\alpha/\beta = 0.5/0.5$, and $\alpha/\beta = 0.7/0.3$, respectively. This indicates that noise-contaminated low-count images suffer from poor lesion visibility, limiting their clinical applicability. Denoising low-count images with the Unet baseline improves corresponding Tversky indexes to 0.64, 0.65, and 0.67, demonstrating the efficacy of DL denoising in boosting lesion visibility. The deployment of the LpQcM further enhances this improvement, elevating Tversky indexes to 0.65, 0.66, and 0.69, thereby reinforcing lesion visibility and clinical utility.

Fig. 3 presents examples of lesion segmentation on low-count and denoised images. Observations from the segmentation network reveal that denoised images processed with the

LpQcM exhibit the greatest similarity to high-count references, ensuring more consistent downstream lesion segmentations. The LpQcM reduces both lesion false negatives (Fig. 3 (a)(c)) and false positives (Fig. 3 (b)(d)) in PET image denoising.

TABLE III Improved lesion visibility in denoised images facilitated by the LpQcM, taking low-count images of 5% count levels as examples.

	Tversky Index		
	$\alpha=0.3, \beta=0.7$	$\alpha=0.5, \beta=0.5$ (Dice)	$\alpha=0.7, \beta=0.3$
low-count	0.3952±0.2737	0.3381±0.2524	0.3014±0.2372
w/o LpQcM	0.6370±0.1939	0.6532±0.1846	0.6744±0.1745
w LpQcM	0.6455±0.1946†	0.6635±0.1821†	0.6879±0.1706†

† $P < 0.05$ based on the non-parametric Wilcoxon signed-rank test between the w/o and w LpQcM groups. (t), (l) and (o) represent expecting higher, lower, and zero-approaching values, respectively.

C. Ablation Studies

To assess the contribution of each component within the LpQcM, ablation studies were conducted, with average results of all cases listed in Table IV. The LpM, with its focus on lesions, reduces quantification biases for lesion SUV_{mean} , SUV_{max} , and TLG by 1.76%, 3.56%, and 0.98% on average, respectively. The LpM shows limited improvements in overall image quality metrics due to the minor proportion of lesions within images. In contrast, the QcM improves quality metrics NRMSE, PSNR, and SSIM, given its emphasis on volume-by-volume radioactivity accuracy across the entire image, though its impact on lesion quantification biases is relatively modest. By combining both components, the LpQcM not only reduces biases in lesion quantification but also improves the fidelity of overall images, surpassing the baseline with a mean reduction of 1.71% in TLG bias and a mean increase of 0.36 in PSNR.

Fig. 4 is the Bland-Altman analysis on the performance of the LpQcM and its ablated versions, assessing the agreement between denoised images and high-count references in calculating TLG. Results show that both the LpM and QcM contribute to a higher agreement between denoised images and references. The LpQcM achieves the highest agreement,

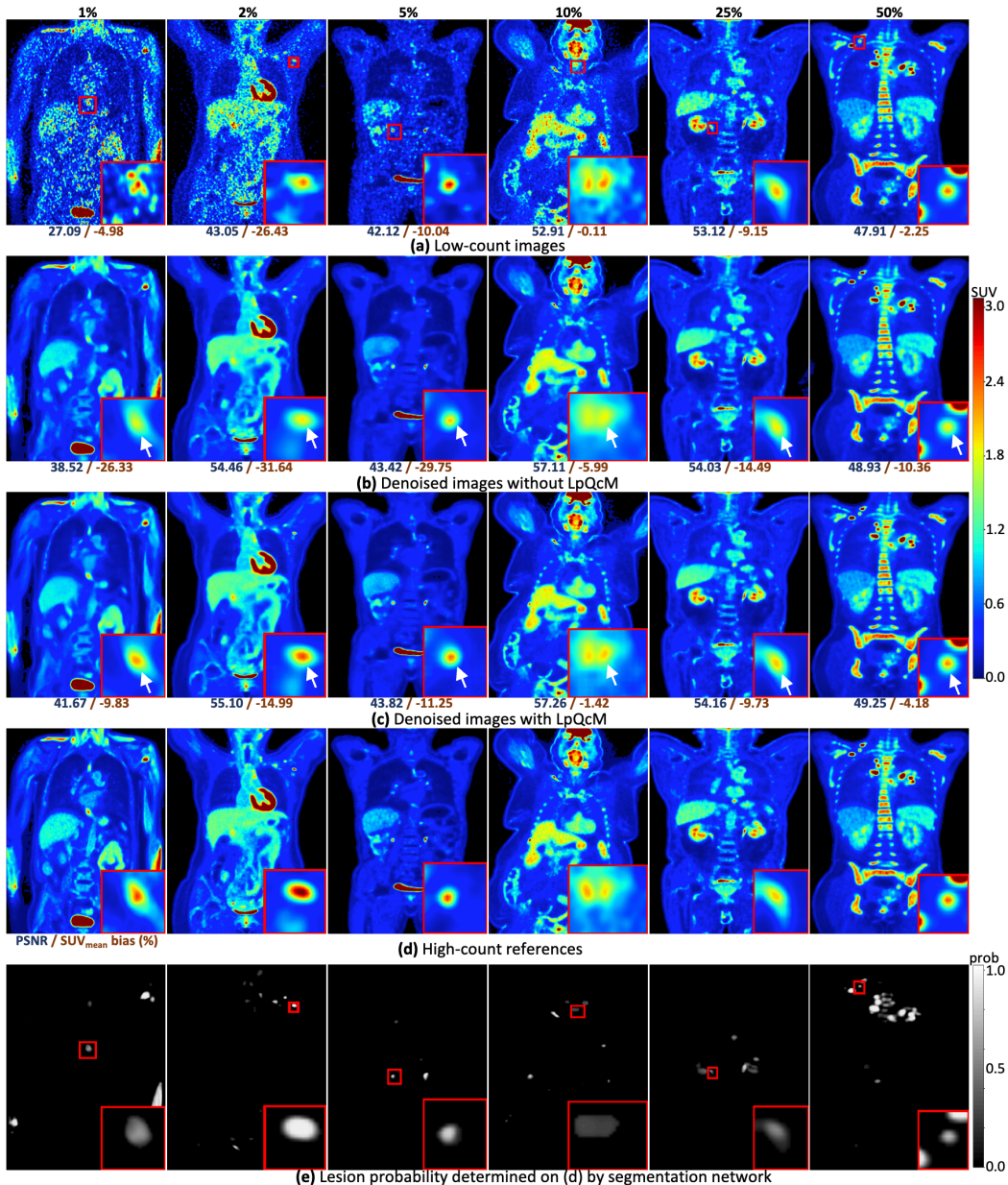


Fig. 2 Visual comparisons of denoised results without and with the LpQcM. Lesion probability maps determined by the auxiliary segmentation network are also displayed for reference. Sub-regions including lesions or lesion-like hot spots are cropped, amplified, and displayed in the bottom-right corner of each image. PSNR and lesion SUV_{mean} bias values are denoted below each image.

outperforming the baseline with a reduction of 0.11 in the average differences.

TABLE IV Ablation studies on the LpQcM with the baseline utilizing Unet.

	NRMSE (*100) (L)	PSNR (T)	SSIM (T)	SUV_{mean} bias (%) (o)	SUV_{max} bias (%) (o)	TLG bias (%) (o)
Baseline	0.339 ± 0.413	52.197 ± 7.094	98.941 ± 2.095	-13.802 ± 18.401	-17.798 ± 21.987	-4.965 ± 6.215
+ LpM	0.331 ± 0.278	52.388 ± 7.067	99.040 ± 1.879	-12.040 ± 17.843	-14.237 ± 21.646	-3.986 ± 6.137
+ QcM	0.322 ± 0.634	52.510 ± 7.137	99.103 ± 1.454	-13.996 ± 18.479	-16.952 ± 21.948	-4.795 ± 6.394
+ LpQcM	0.314 ± 0.279	52.555 ± 7.156	99.135 ± 1.378	-11.895 ± 15.366	-13.744 ± 19.547	-3.257 ± 5.668

(T), (L) and (o) represent expecting higher, lower, and zero-approaching values, respectively.

D. Adaptability to Various Architectures

Beyond its effectiveness on the Unet baseline, the LpQcM shows flexible adaptability to a variety of denoising

frameworks. Table V summarizes the performance of the LpQcM on SwinUNETR and GAN architectures, indicating enhancements in both image quality and lesion quantification metrics. Specifically, the LpQcM facilitates an average TLG bias reduction of 1.04% for GAN and 1.44% for SwinUNETR baselines.

For more intuitive comparisons, Fig. 5 employs boxplots to depict lesion quantification accuracy across different architectures with and without the LpQcM. In every scenario, setups incorporating the LpQcM outperform those without, with the GAN enhanced by LpQcM leading in overall performance. Further, Fig. 6 presents a visual comparison of denoising outcomes from various models, clearly demonstrating that the LpQcM improves denoising performance across multiple baseline models.

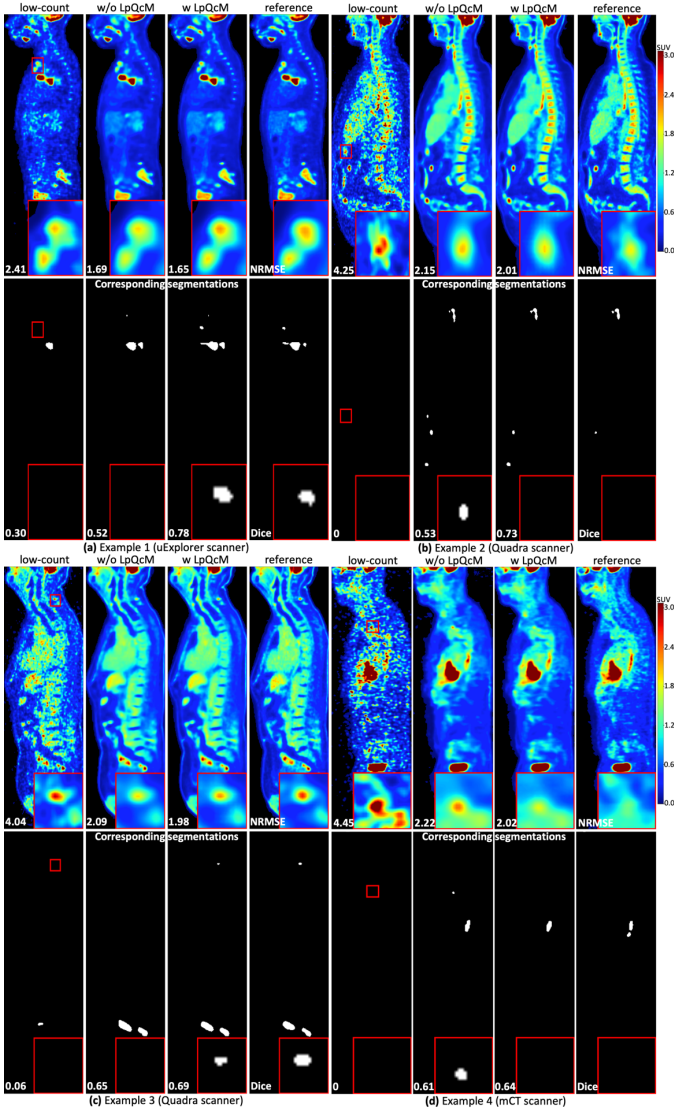


Fig. 3 Examples of lesion segmentation on low-count, denoised, and high-count images. Lesion probability maps output by the segmentation network were binarized by 0.5 to obtain lesion segmentation masks. Sub-regions of interest were cropped, amplified, and displayed in the bottom-right corner of each image. NRMSE value and Dice coefficient are denoted in white text.

TABLE V Adaptability of the LpQcM to various denoising baselines.

		GAN				SwinUNETR			
		NRMSE		TLG bias		NRMSE		TLG bias	
		(*)	(L)	(%)	(o)	(*)	(L)	(%)	(o)
Quadra	1%	0.2731	0.2659[†]	-5.1147	-4.4436[†]	0.2944	0.2841[†]	-7.3947	-5.3036[†]
	2%	0.2523	0.2335[†]	-4.0920	-3.3757[†]	0.2399	0.2305[†]	-5.6170	-3.8889[†]
	5%	0.1956	0.1944	-2.5917	-2.3280[†]	0.2073	0.2164	-4.2442	-2.9804[†]
	10%	0.1784	0.1686[†]	-1.7870	-1.5828[†]	0.1844	0.1803	-3.3118	-2.1329[†]
	25%	0.1462	0.1312[†]	-1.0347	-0.8788[†]	0.1726	0.1367[†]	-2.1926	-1.1631[†]
uExplorer	1%	0.5505	0.5357[†]	-13.2311	-9.6707[†]	0.5738	0.5548[†]	-15.3542	-13.5858[†]
	2%	0.4390	0.4321[†]	-8.6013	-6.6957[†]	0.4527	0.4396[†]	-11.2858	-8.9291[†]
	5%	0.3540	0.3531[†]	-4.8685	-4.1634[†]	0.3712	0.3487[†]	-7.0689	-5.0798[†]
	10%	0.2836	0.2740[†]	-3.2847	-3.0921[†]	0.3025	0.2944[†]	-5.3705	-3.6718[†]
	25%	0.2133	0.2240	-1.8003	-1.6793[†]	0.2313	0.2255[†]	-3.7206	-2.2488[†]
mCT	50%	0.1532	0.1421[†]	-1.0155	-1.0282	0.1821	0.1654[†]	-2.8045	-1.3508[†]
	5%	0.5376	0.5271[†]	-6.0240	-4.5033[†]	0.5305	0.5243[†]	-6.9250	-6.2317[†]
	10%	0.5230	0.4490[†]	-4.1865	-3.6721[†]	0.4585	0.4302[†]	-5.1353	-4.3532[†]
	20%	0.3437	0.3391[†]	-2.7826	-1.8186[†]	0.3606	0.3477[†]	-3.9980	-3.2077[†]

[†] P-value <0.05 based on the non-parametric Wilcoxon signed-rank test between the w/o and w LpQcM groups.

(L) and (o) represent expecting lower and zero-approaching values, respectively.

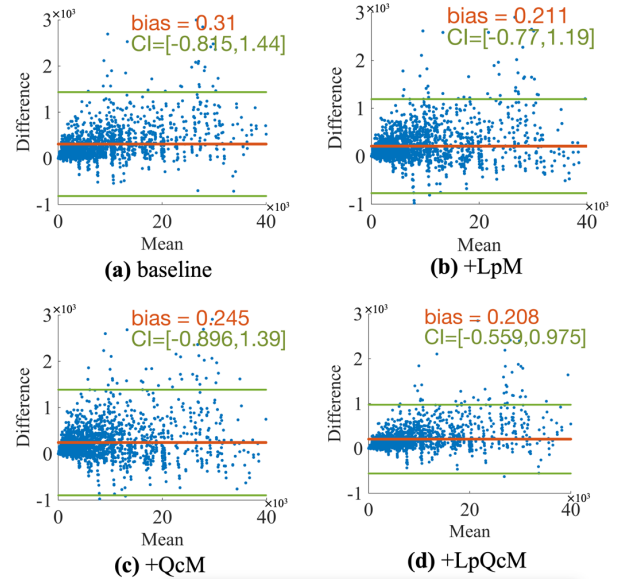


Fig. 4 Bland-Altman analysis on the performance of the LpQcM and its ablated versions, in terms of quantifying the TLG. The y-axis represents the bias between TLG values measured by denoised images and high-count references. The x-axis represents the average TLG values obtained from the denoised and reference images. The mean bias is highlighted by a red line. The 96% confidence intervals (CI) of the bias are indicated by green lines.

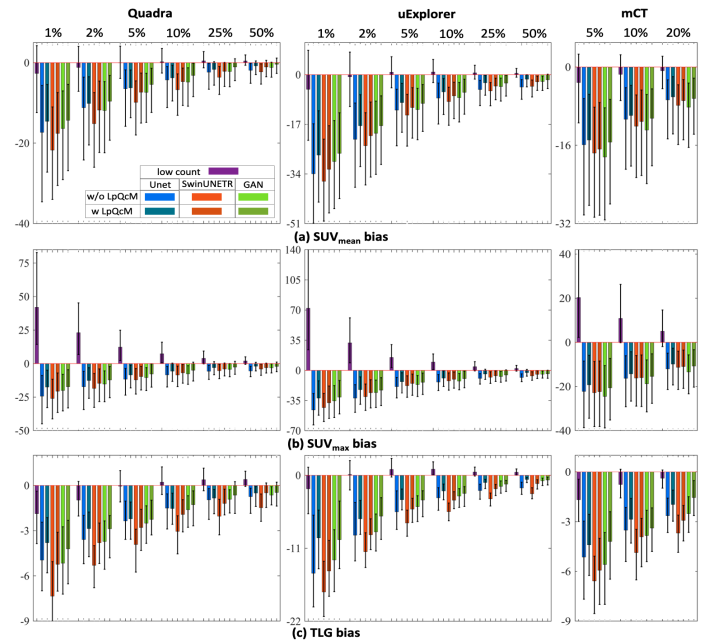


Fig. 5 Boxplots on LpQcM performance across various denoising architectures, in terms of (a) SUV_{mean} bias, (b) SUV_{max} bias, and (c) TLG bias.

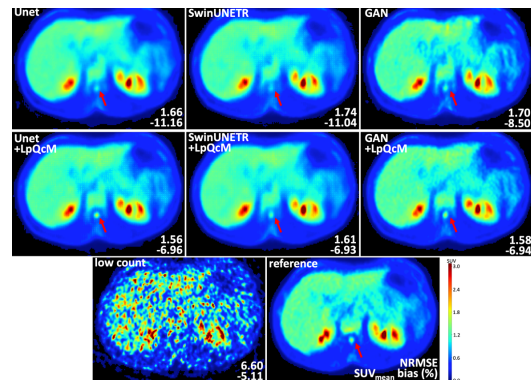


Fig. 6 Adaptability of the LpQcM to different denoising architectures.

V. DISCUSSION

The LpQcM introduces innovative ideas to develop clinically reliable and practically viable DL models for denoising low-count PET images. **(1)** From a clinical perspective, the paramount attributes of denoised images are lesion visibility and quantification accuracy. Previous DL denoising models [26]-[24] for PET have focused on producing visually striking images, thereby enhancing overall image quality metrics like PSNR and SSIM. They often overlook the clinical utility of denoised images for subsequent lesion analysis and diagnosis. While these methods yield high-resolution images, the potential loss of lesions and biased radioactivity quantification in denoised outputs compromise the DL credibility for clinical uses. The LpQcM pioneered in integrating lesion segmentation and multiscale quantification to assist PET image denoising, with an emphasis on factors essential for clinical evaluation. Consequently, it improves lesion contrast and visibility in denoised images and elevates quantification accuracy for clinical metrics such as SUV_{mean} , SUV_{max} , and TLG, as evidenced in Table II and III and Fig. 2 and 3. Compared to the baseline, integrating the LpQcM results in a 1.71% decrease in TLG bias and a 1.58% improvement in Dice coefficient for downstream lesion segmentation. **(2)** From a practical perspective, earlier segmentation-assisted denoising models [27]-[29] have typically integrated semantic contexts by adding extra convolutional layers into denoising architectures, which leads to a marked increase in computational complexity. They require manually preparing segmentation labels matched to noisy-clean image pairs in denoising datasets. In contrast, the LpQcM enhances denoising performance without adding computational burden to model inference, by modulating data distributions and optimization processes during model training. It decouples the auxiliary lesion segmentation from the main denoising architecture and leverages public data sources to pre-train segmentation network, thereby avoiding manual lesion label requirements matched to low- and high-count images in denoising datasets. These designs make the LpQcM a highly adaptable, plug-and-play module that is compatible with various denoising architectures. Shown in Table V and Fig. 5 and 7, the LpQcM improves denoising performance across different baselines, including Unet, SwinUNETR, and GAN. On average, the LpQcM reduces lesion SUV_{max} bias by 4.93%, 2.05%, and 2.53% for Unet, SwinUNETR, and GAN, respectively.

The LpQcM benefits from and is characterized by its two components, the LpM and the QcM. **(1)** The LpM is inspired by active learning principles [38]. Active learning strategically selects the most informative and representative data samples for annotating and model learning, which enhances model performance while minimizing labeling and training expenses. This approach is particularly valuable in addressing imbalances by prioritizing informative but numerically inferior samples. In the context of PET image denoising, lesion-present samples are more representative but less numerous. At the patch level, lesion-absent patches significantly outnumber those containing lesions. At the voxel level, lesion voxels are less common than

non-lesion ones. To counteract these imbalances, the LpM performs active learning in forms of patch-level lesion-perceived sampling and voxel-level lesion-perceived consistency. The former adjusts training data distributions to mitigate patch-level imbalances, selecting patches based on the segmentation network’s confidence in lesion presence. The latter modifies loss functions to concentrate on lesional voxels identified by the segmentation network. Importantly, the LpM utilizes continuous segmentation probabilities instead of binary segmentation masks thresholded at 0.5, allowing for more nuanced modulation on denoising training and reducing the dependency on segmentation accuracy. As a result, the LpM has been shown to improve lesion quantification accuracy, with reductions of 1.76%, 3.56%, and 0.98% in SUV_{mean} bias, SUV_{max} bias, and TLG bias, respectively, as detailed in Table IV and Fig. 4. **(2)** Beyond focusing on lesions, the QcM extends to ensure the accuracy of SUV_{mean} and SUV_{max} quantification across multiscale ROIs throughout the entire image. Given the importance of precise radioactivity quantification in anatomical organs and the common lack of image-aligned organ labels, the QcM employs sub-volumes of varying sizes to mimic anatomical semantics, representing the image as a collection of volumetric ROIs. Then, the QcM enforces quantification accuracy within each ROI at every scale, with the strictest standards at the finest scale. By imposing constraints across the whole image scope, the QcM enhances image fidelity and mitigates over-smoothing, improving NRMSE, PSNR, and SSIM by 0.02, 0.41, and 0.16, respectively, and also offers modest reductions in lesion quantification biases, as demonstrated in Table IV and Fig. 4.

Although the LpQcM has shown promising outcomes, there remains substantial space for further advancement. **(1)** The auxiliary segmentation network within LpQcM, while effective, has limitations in its ability to comprehensively identify lesions. It has been trained on the public dataset [34] of a single scanner featuring tumors of malignant melanoma, lymphoma, and lung cancer. Despite a degree of generalizability to other lesions through patch-wise processing, the risk of missing certain lesion types in denoising datasets weakens its support for denoising. Future versions should aim to encompass wider types of tumors and scanners. And the approach of categorizing each lesion type distinctly, rather than merely differentiating lesion presence and absence, deserves additional exploration. **(2)** While LpQcM benefits from decoupling auxiliary segmentation from primary denoising, thereby relaxing dataset requirements, approaches that foster greater dual-task cooperation may offer enhanced mutual benefits, assuming suitable datasets are accessible. Moreover, incorporating anatomical organ semantics from modalities such as CT or MRI, in addition to metabolic lesion knowledge, potentially provides stronger support for denoising. **(3)** Further experimental work with the LpQcM can explore datasets utilizing a wider variety of radiotracers beyond FDG, as well as more types of DL models such as diffusion models. Such exploration may reveal new insights into method effectiveness and versatility.

VI. CONCLUSION

We present a lesion-quantification-consistent modulation strategy named the LpQcM, for enhancing low-count PET image denoising with a focus on lesion visibility and precise multiscale radioactivity quantification. We validate the efficacy of each innovation and prove that the LpQcM contributes to improved lesion quantification accuracy and overall image quality. The LpQcM strategy, facilitated by downstream analysis, delivers considerable clinical and practical benefits.

REFERENCES

- [1] P. E. Valk, D. L. Bailey, D. W. Townsend, and M. N. Maisey, "Positron emission tomography," *Springer-Verlag London*, vol. 1, p. 5, 2003.
- [2] S. L. Kitson, V. Cuccurullo, A. Ciarmiello, D. Salvo, and L. Mansi, "Clinical applications of positron emission tomography (PET) imaging in medicine: oncology, brain diseases and cardiology," *Current Radiopharmaceuticals*, vol. 2, no. 4, pp. 224-253, 2009.
- [3] K. J. Strauss and S. C. Kaste, "The ALARA (as low as reasonably achievable) concept in pediatric interventional and fluoroscopic imaging: striving to keep radiation doses as low as possible during fluoroscopy of pediatric patients - a white paper executive summary," *Radiology*, vol. 240, no. 3, pp. 621-622, 2006.
- [4] A. Bousse *et al.*, "A review on low-dose emission tomography post-reconstruction denoising with neural network approaches," *IEEE Transactions on Radiation and Plasma Medical Sciences*, 2024.
- [5] J. Dutta, R. M. Leahy, and Q. Li, "Non-local means denoising of dynamic PET images," *PloS one*, vol. 8, no. 12, p. e81390, 2013.
- [6] H. Arabi and H. Zaidi, "Non-local mean denoising using multiple PET reconstructions," *Annals of Nuclear Medicine*, vol. 35, pp. 176-186, 2021.
- [7] F. E. Turkheimer *et al.*, "PET image denoising using a synergistic multiresolution analysis of structural (MRI/CT) and functional datasets," *Journal of Nuclear Medicine*, vol. 49, no. 4, pp. 657-666, 2008.
- [8] J. M. Mejia *et al.*, "Noise reduction in small-animal PET images using a multiresolution transform," *IEEE Transactions on Medical Imaging*, vol. 33, no. 10, pp. 2010-2019, 2014.
- [9] A. Le Pogam *et al.*, "Denoising of PET images by combining wavelets and curvelets for improved preservation of resolution and quantitation," *Medical Image Analysis*, vol. 17, no. 8, pp. 877-891, 2013.
- [10] F. Hashimoto, Y. Onishi, K. Ote, H. Tashima, A. J. Reader, and T. Yamaya, "Deep learning-based PET image denoising and reconstruction: a review," *Radiological Physics and Technology*, pp. 1-23, 2024.
- [11] Q. Liu *et al.*, "A personalized deep learning denoising strategy for low-count PET images," *Physics in Medicine & Biology*, vol. 67, no. 14, p. 145014, 2022.
- [12] G. Angelis, O. Fuller, J. Gillam, and S. Meikle, "Denoising non-steady state dynamic PET data using a feed-forward neural network," *Physics in Medicine & Biology*, vol. 66, no. 3, p. 034001, 2021.
- [13] S. Y. Yie, K. M. Kim, S. Bae, and J. S. Lee, "Effects of loss functions and supervision methods on total-body PET denoising," *IEEE Transactions on Radiation and Plasma Medical Sciences*, 2023.
- [14] S. Xue *et al.*, "A cross-scanner and cross-tracer deep learning method for the recovery of standard-dose imaging quality from low-dose PET," *European Journal of Nuclear Medicine and Molecular Imaging*, pp. 1-14, 2021.
- [15] S.-I. Jang *et al.*, "Spach transformer: spatial and channel-wise transformer based on local and global self-attentions for PET image denoising," *IEEE Transactions on Medical Imaging*, 2023.
- [16] Y. Li *et al.*, "A noise-level-aware framework for PET image denoising," in *International Workshop on Machine Learning for Medical Image Reconstruction*, 2022, pp. 75-83.
- [17] H. Xie *et al.*, "Unified noise-aware network for low-count PET denoising with varying count levels," *IEEE Transactions on Radiation and Plasma Medical Sciences*, 2023.
- [18] B. Zhou *et al.*, "FedFTN: Personalized federated learning with deep feature transformation network for multi-institutional low-count PET denoising," *Medical Image Analysis*, vol. 90, p. 102993, 2023.
- [19] Y. He *et al.*, "Dynamic PET image denoising with deep learning-based joint filtering," *IEEE Access*, vol. 9, pp. 41998-42012, 2021.
- [20] M. Fu *et al.*, "OIF-Net: An optical flow registration-based PET/MR cross-modal interactive fusion network for low-count brain PET image denoising," *IEEE Transactions on Medical Imaging*, 2023.
- [21] Q. Zhang *et al.*, "Deep generalized learning model for PET image reconstruction," *IEEE Transactions on Medical Imaging*, 2023.
- [22] Z. Han *et al.*, "Contrastive diffusion model with auxiliary guidance for coarse-to-fine PET reconstruction," in *International Conference on Medical Image Computing and Computer-Assisted Intervention*, 2023, pp. 239-249.
- [23] K. Gong, K. Johnson, G. El Fakhri, Q. Li, and T. Pan, "PET image denoising based on denoising diffusion probabilistic model," *European Journal of Nuclear Medicine and Molecular Imaging*, pp. 1-11, 2023.
- [24] C. Shen, Z. Yang, and Y. Zhang, "PET image denoising with score-based diffusion probabilistic models," in *International Conference on Medical Image Computing and Computer-Assisted Intervention*, 2023, pp. 270-278.
- [25] M. Loft *et al.*, "An investigation of lesion detection accuracy for artificial intelligence-based denoising of low-dose ⁶⁴Cu-DOTATATE PET imaging in patients with neuroendocrine neoplasms," *Journal of Nuclear Medicine*, vol. 64, no. 6, pp. 951-959, 2023.
- [26] W. Lu *et al.*, "An investigation of quantitative accuracy for deep learning-based denoising in oncological PET," *Physics in Medicine & Biology*, vol. 64, no. 16, p. 165019, 2019.
- [27] Z. Huang *et al.*, "Segmentation-guided denoising network for low-dose CT imaging," *Computer Methods and Programs in Biomedicine*, vol. 227, p. 107199, 2022.
- [28] Z. Huang *et al.*, "Learning a deep CNN denoising approach using anatomical prior information implemented with attention mechanism for low-dose CT imaging on clinical patient data from multiple anatomical sites," *IEEE Journal of Biomedical and Health Informatics*, vol. 25, no. 9, pp. 3416-3427, 2021.
- [29] Z. Huang *et al.*, "Considering anatomical prior information for low-dose CT image enhancement using attribute-augmented Wasserstein generative adversarial networks," *Neurocomputing*, vol. 428, pp. 104-115, 2021.
- [30] T.-O. Buchholz, M. Prakash, D. Schmidt, A. Krull, and F. Jug, "DenoiSeg: joint denoising and segmentation," in *European Conference on Computer Vision*, 2020, pp. 324-337.
- [31] O. C. İc ek, A. Abdulkadir, S. S. Lienkamp, T. Brox, and O. Ronneberger, "3D U-net: learning dense volumetric segmentation from sparse annotation," in *Medical Image Computing and Computer-Assisted Intervention*, 2016, pp. 424-432.
- [32] H. H. Chen, N.-T. Chiu, W.-C. Su, H.-R. Guo, and B.-F. Lee, "Prognostic value of whole-body total lesion glycolysis at pretreatment FDG PET/CT in non-small cell lung cancer," *Radiology*, vol. 264, no. 2, pp. 559-566, 2012.
- [33] J.-Y. Zhu, T. Park, P. Isola, and A. A. Efros, "Unpaired image-to-image translation using cycle-consistent adversarial networks," in *IEEE International Conference on Computer Vision*, 2017, pp. 2223-2232.
- [34] S. Gatidis *et al.*, "A whole-body FDG-PET/CT dataset with manually annotated tumor lesions," *Scientific Data*, vol. 9, no. 1, p. 601, 2022.
- [35] A. Gnanasambandam and S. Chan, "One size fits all: Can we train one denoiser for all noise levels?" in *International Conference on Machine Learning*, 2020, pp. 3576-3586.
- [36] A. Hatamizadeh *et al.*, "SwinUNETR: Swin transformers for semantic segmentation of brain tumors in MRI images," in *International MICCAI Brainlesion Workshop*, 2021, pp. 272-284.
- [37] S. Kollem, K. R. L. Reddy, and D. S. Rao, "A review of image denoising and segmentation methods based on medical images," *International Journal of Machine Learning and Computing*, vol. 9, no. 3, pp. 288-295, 2019.
- [38] U. Aggarwal, A. Popescu, and C. Hudelot, "Active learning for imbalanced datasets," in *IEEE/CVF Winter Conference on Applications of Computer Vision*, 2020, pp. 1428-1437.